

# All-Optical tunability of metalenses permeated with liquid crystals

Giovanna Palermo,<sup>†,#</sup> Andrew Lininger,<sup>‡,#</sup> Alexa Guglielmelli,<sup>†</sup> Loredana Ricciardi,<sup>¶</sup> Giuseppe Nicoletta,<sup>†</sup> Antonio De Luca,<sup>§</sup> Joon-Suh Park,<sup>||,⊥</sup> Soon Wei Daniel Lim,<sup>||</sup> Maryna L. Meretska,<sup>||</sup> Federico Capasso,<sup>\*,||</sup> and Giuseppe Strangi<sup>\*,‡,†</sup>

<sup>†</sup>*Department of Physics, NLHT-Lab, University of Calabria and CNR-NANOTEC Istituto di Nanotecnologia, 87036-Rende, Italy*

<sup>‡</sup>*Department of Physics, Case Western Reserve University, 2076 Adelbert Rd, Cleveland, Ohio 44106, USA*

<sup>¶</sup>*CNR-NANOTEC Istituto di Nanotecnologia, 87036-Rende, Italy*

<sup>§</sup>*Department of Physics, University of Calabria and CNR-NANOTEC Istituto di Nanotecnologia, 87036-Rende, Italy*

<sup>||</sup>*Harvard John A. Paulson School of Engineering and Applied Sciences, Harvard University, Cambridge, MA 02138, USA*

<sup>⊥</sup>*Nanophotonics Research Centre, Korea Institute of Science and Technology, Seoul 02792, Republic of Korea*

*#Contributed equally to this work*

<sup>\*</sup> E-mail: capasso@seas.harvard.edu

<sup>\*</sup> Email giuseppe.strangi@case.edu

## Contents:

- Schematic diagram of the optical setup used to characterize the focal spot and the intensity distribution of the metlens.

- Temperature-dependent refractive indices of 6CB at  $\lambda=589$  nm.
- Synthesis and characterization of the AuNPs.
- Photothermal characterization of the AuNPs.
- Schematic diagram of the full experimental apparatus.
- Experimental and theoretical modulation transfer function comparison.
- Simulation procedures.
- Mechanism of coexisting phase profiles.
- Manipulating the focal point tunability range by varying the infiltrate refractive index.
- Experimental estimation of the infiltrated liquid crystal thickness.
- Comparison with some other similar tunable metalens systems.

## Schematic diagram of the optical setup used to characterize the focal spot and the intensity distribution of the metalens.

A continuous red laser (He-Ne, JDS Uniphase 1137P,  $\lambda=633$  nm) is used to illuminate the metalens. A  $\lambda/2$  waveplate and linear polarizer are used to control the intensity of the laser to avoid saturating the CCD (Pixelfly-Qe, high performance, digital 12 bit). To fully illuminate the metalens, the laser beam is enlarged with a beam expander (beam diameter  $\sim 1$  cm). The resulting focal profile, after passing through the metalens, is collected with a 50X objective (Leica 566040, N.A.= 0.5) and impinges through a tube lens on the CCD camera, that are mounted on a z-axis translation stage controlled by a stepper motor.

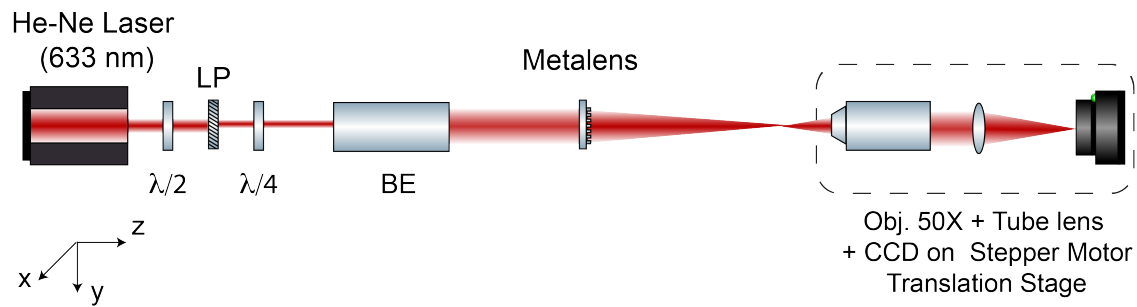


Figure S1: Schematic diagram of the metalens focal profile characterization optical apparatus. The objective - CCD setup is moved sequentially along the optical axis to collect the full focal profile.

## Temperature-dependent refractive indices of 6CB at $\lambda=589$ nm.

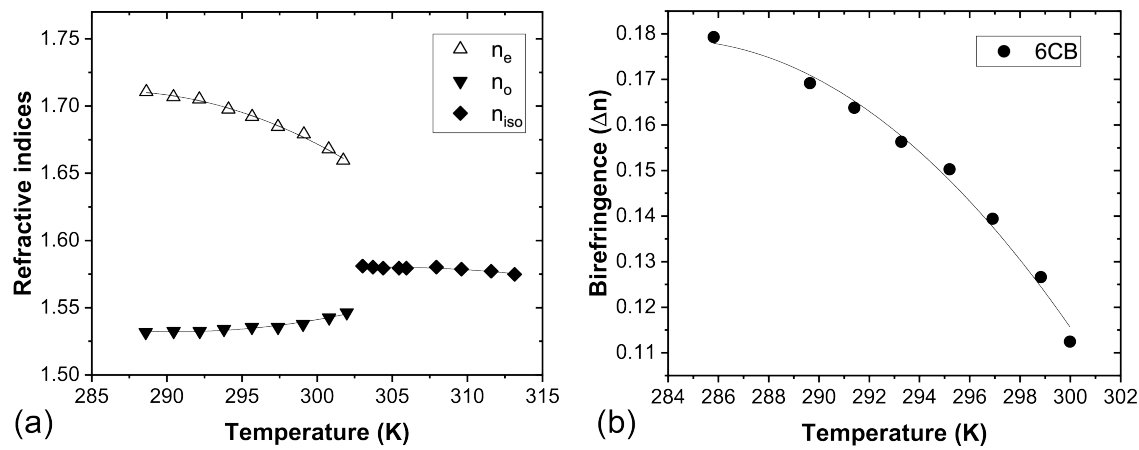


Figure S2: (a) Temperature-dependent refractive indices of 6CB at  $\lambda=589$  nm. (b) Temperature-dependent birefringence of 6CB at  $\lambda=589$  nm.<sup>1</sup>

## Synthesis and characterization of the AuNPs.

**Chemicals.** Hydrogen tetrachloroaurate(III) trihydrate ( $\text{HAuCl}_4 \cdot 3\text{H}_2\text{O}$ ), trisodium citrate, and polyvinilpyrrolidone (PVP, average MW 10,000 g/mol) were purchased from Sigma-Aldrich. All solutions were prepared using distilled water.

**Synthesis.** The citrate-stabilized AuNPs with an average diameter of  $34 \pm 2$  nm were synthesized following the well-developed kinetically controlled seeded growth method,<sup>2</sup> via the reduction of  $\text{HAuCl}_4$  by sodium citrate. Briefly, the gold seeds (~10 nm) were prepared by adding 1 mL of  $\text{HAuCl}_4$  (25 mM) into 150 mL of reducing solution containing sodium citrate (2.2 mM) at 100 °C under reflux and vigorous stirring. Within 10 min the solution turned from pale yellow to blue-gray, pink, and then wine-red indicating the colloidal nanoparticles formation. To halt further growth steps, the temperature of the solution was decreased to 90 °C in order to prevent any secondary nucleation process. Then, 1 mL of sodium citrate (60 mM) and 1 mL of  $\text{HAuCl}_4$  (25 mM) were sequentially injected, and the reaction was run for 30 min. This step was repeated four times. Then, the sample was diluted by extracting 55 mL of sample and adding 53 mL of water and 2 mL of 60 mM sodium citrate. 1 mL of 25 mM  $\text{HAuCl}_4$  was injected after 1 min and 1 mL after 30 min. Then, the reaction was run for 30 min. This step was repeated two times. Finally, 2.5 mL of 3.3 mM PVP were added to the AuNPs solution and kept under stirring for 24 h. The so-synthesized AuNPs were purified by ultrafiltration method (Vivaspin®20 equipped with a 100 kDa membrane) and then dispersed in spectrofluorimetric grade ethanol obtaining a final concentration of 2 nM.

**Characterization.** UV-visible extinction spectra were recorded using a Perkin Elmer Lambda 900 spectrophotometer. The morphology of the synthesized nanoparticles was observed by using a JEOL 2010F transmission electron microscope (TEM). The sample was prepared by depositing a drop of a diluted colloidal solution on 200 mesh carbon-coated copper grids. After evaporation of the solvent in air at room temperature, the particles were observed at an operating voltage of 80 kV. Size distribution measurements were performed in triplicate at 25 °C by using a Zetasizer Nano ZS system from Malvern Instruments (632.8 nm, 4 mW HeNe gas laser, avalanche photodiode detector, 175° detection).

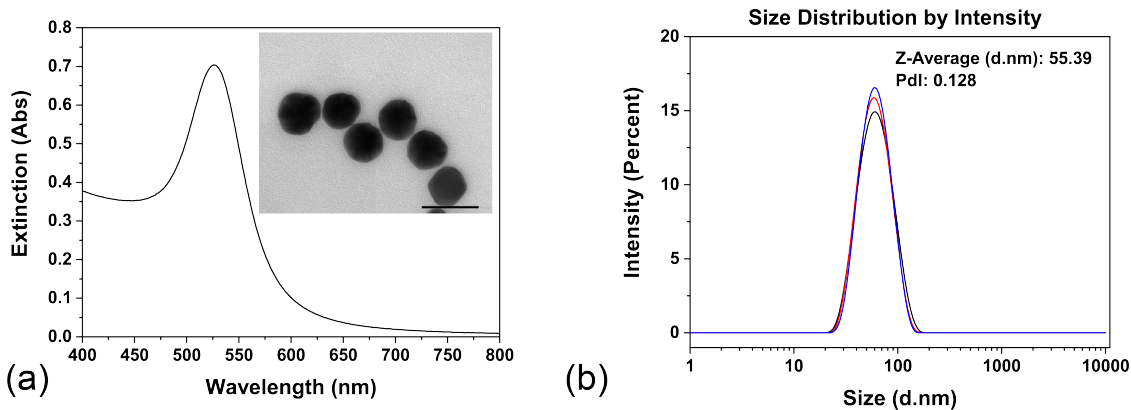


Figure S3: (a) Extinction spectrum of AuNPs in water solution. In the inset, TEM image of AuNPs. Scale bar: 50 nm. (b) Hydrodynamic size and size distribution of AuNPs.

### Photothermal characterization of the AuNPs.

To characterize the photothermal effects of the metallic colloidal solution, the solution is loaded into a 10 mm quartz cuvette and exposed to a resonant CW green laser ( $\lambda = 532$  nm), impinging perpendicularly to it. In this way the heating phenomena related to the excitation of the LSPR has been stimulated. The thermal effect strongly depends on the resonant pump beam intensity  $I$  (power/surface); in fact, the energy absorbed (and delivered) by a single AuNP, which transforms in a dissipated heat  $Q$  from the nanoparticle, can be simply expressed as a function of the absorption cross section  $\sigma_{abs}$  and the impinging intensity  $I$ :  $Q = \sigma_{abs} I$ . The thermographic analysis reveals the presence of hot spots, related to the photoinduced heat generated by the AuNPs. By monitoring the temperature values of the central pixel area of each hot spot, corresponding to the warmest point, it is possible to plot the temperature increase  $\Delta T = T - T_0$  versus the impinging intensity ( $T_0$  is the temperature when the pump beam is off, which corresponds to room temperature). Experimental data of  $\Delta T$  as a function of the impinging light intensity ranging from 1.0 to 10.0 W/cm<sup>2</sup> are reported in Figure S4. The maximum temperature increase obtained for the  $I_{max} \sim 10$  W/cm<sup>2</sup> is  $\sim 18^\circ\text{C}$ .

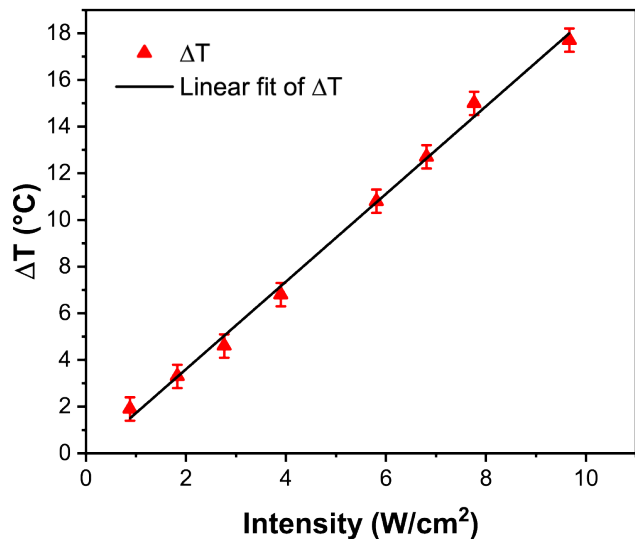


Figure S4: Temperature increase of AuNPs solution as a function of different intensity values of the resonant pump beam.

## Schematic diagram of the full optical experimental apparatus for imaging measurements.

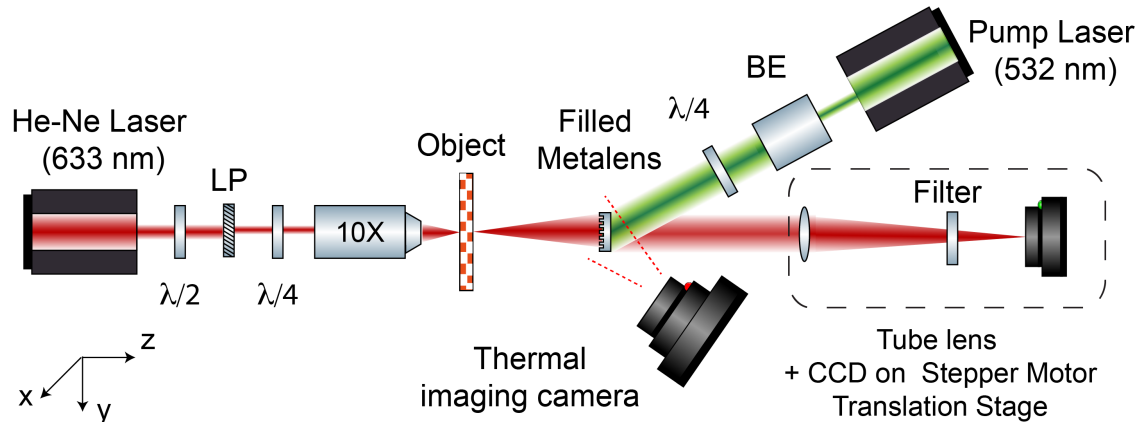


Figure S5: Schematic diagram of the all-optical pump probe - thermographic imaging setup. The metalens is pumped via a continuous 532 nm green laser, as described in the text. A thermal imaging camera is used to monitor the metalens temperature.

## Experimental and theoretical modulation transfer function comparison

The modulation transfer function (MTF) was calculated for each of the PSF profiles shown in the main text, including both the experimental and theoretical PSFs. Broadly, the MTF results show sub-optimal focusing properties of the metalens+NLC system when compared with the near diffraction limited behavior of the uninfiltrated metalens. The decreased focusing properties are consistent between the theoretical and experimental PSFs, indicating that the decreased focusing is a result of the disruption of the target phase profile in the fabricated metalens.

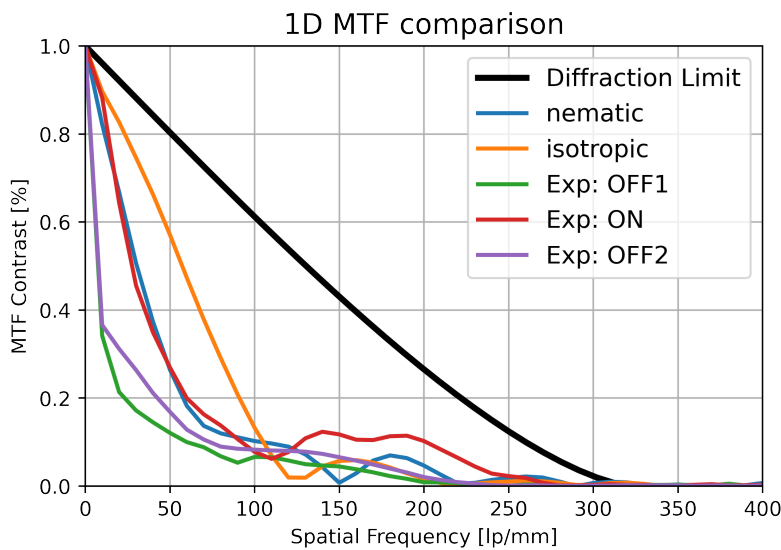


Figure S6: 1D comparison of the modulation transfer function (MTF) for all PSFs presented in the manuscript, including: the theoretical diffraction limit, simulated nematic LC infiltration, simulated isotropic LC infiltration, and experimental PSFs ('Exp') with the beam off (pre-pump), on, and off (post-pump). The 1D representation is exact for the simulated PSFs since the profile is radially symmetric and represents an average of line cuts for the experimental PSFs.

## Simulation procedures

All simulations were performed via a finite difference time domain method solver (MEEP).<sup>3</sup> Individual pillars were simulated with each unique combination of pillar radius, period, height, and liquid crystal infiltration. The glass structure was modeled at the refractive index of the glass ( $n=1.535$ ). The liquid crystal was experimentally confirmed to be in a tangential planar configuration (the director curls in the plane of the pillars following the fabricated circumferential profile of the metalens), therefore the liquid crystal + AuNP mixture was modeled as an isotropic fluid with refractive index equal to the ordinary (or isotropic) refractive index for CB6 ( $n=1.53$  or  $n=1.58$ ). Since the filling fraction of AuNP is small (1%) and the simulations were performed away from the plasmonic resonance, the effect of AuNPs on the effective refractive index was ignored. Periodic boundary conditions were utilized for the in-plane simulation domain boundaries, and perfectly matched layers were employed along the z-axis (optical axis). A plane wave gaussian source centered at 633nm was utilized as the exciting source, and the transmitted fields were monitored at a plane 1266nm ( $2\lambda$ ) above the top of the pillar, in free space. An eigenmode decomposition was then performed to calculate the complex transmitted field in terms of amplitude and phase. A comparison of the transmitted phase relative to the glass substrate for all unique pillar combinations and several infiltration scenarios is shown in **Figure S7**, for the refractive indices 1.53 (a-f) and 1.58 (g-l), respectively. The phase transmission depends strongly on the pillar diameter but less so on the period. The individual pillar simulations were then composed into an overall near-field map of the metalens by mapping the unique pillar and infiltration combinations to the fabrication masking array and assumed liquid crystal infiltration profile. Different liquid crystal orientational states and infiltration profiles can then be investigated by simulating the refractive index shift and rearranging the simulation mapping. Individual pillar simulations were performed for all unique combinations of pillar radius and period, as well as both the ordinary and isotropic refractive indices of the infiltrated liquid crystal ( $n=1.53$  or  $n=1.58$ ) with infiltration heights in the range of 0.01 to  $1.25 \mu\text{m}$  in steps of 50nm. Accuracy could be improved by increasing the number of simulated depths to better approximate smooth infiltration profiles; in the current results the

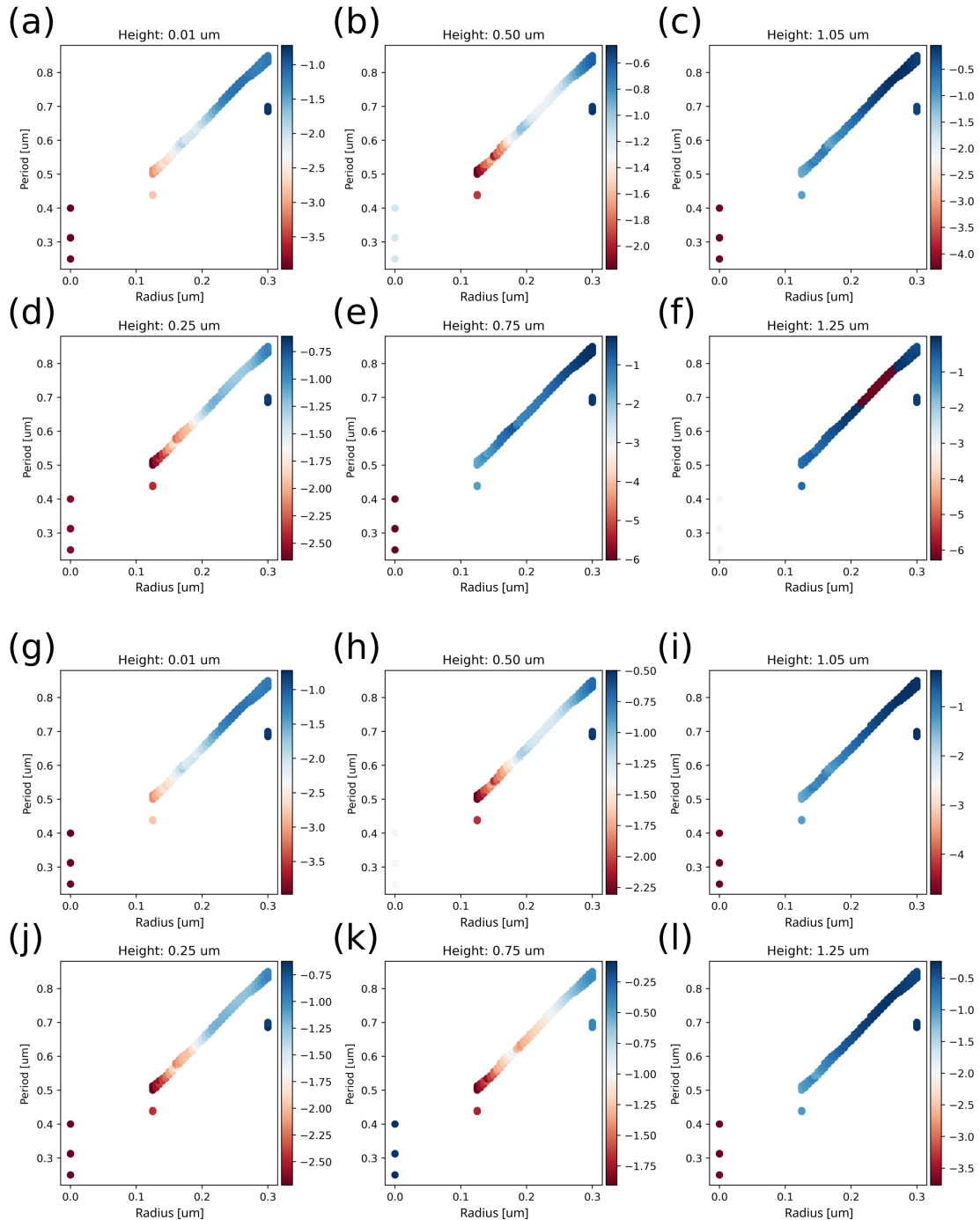


Figure S7: Simulated phase transmission for a wide variety of pillar properties and infiltration levels. The phase transmission (color) is shown for pillars as a function of radius and period. **(a-f)** Ordinary (1.53) refractive index infiltration at various depths. **(g-l)** Isotropic (1.58) refractive index infiltration at various depths. The refractive index is shown to slightly affect the phase transmission, with a major effect from varying the depth. Infiltrated liquid crystal is also seen to affect the range of available phases.

simulated infiltration depth is accurate to 50nm.

The transmitted near-field phase profile is important for the manipulation of the far field profile. Some sample near-field phase profiles are shown in **Figure S8** for the ‘empty’ metalens, a constant infiltration height of 0.25um at the ordinary and isotropic refractive indices, and the quadratic radial infiltration profile described in the main text. These profiles only cover the central region of the metalens, with the outer regions omitted for clarity. Comparing the empty and radial infiltrated phase profiles, it is clear that the central region has a largely unchanged phase, although differences can be detected along the edges. It should be noted that the amplitude of the phase profile is greatly depressed for most infiltration scenarios. This is because the addition of liquid crystal near the pillar decreases the index contrast (and nearly erases it for the ordinary refractive index) for some portion of the pillar height. Given that the pillar geometry is fixed at the time of fabrication, this implies that the phase profile will be disrupted and typically diminished from the optimized phase profile inherent in the empty lens.

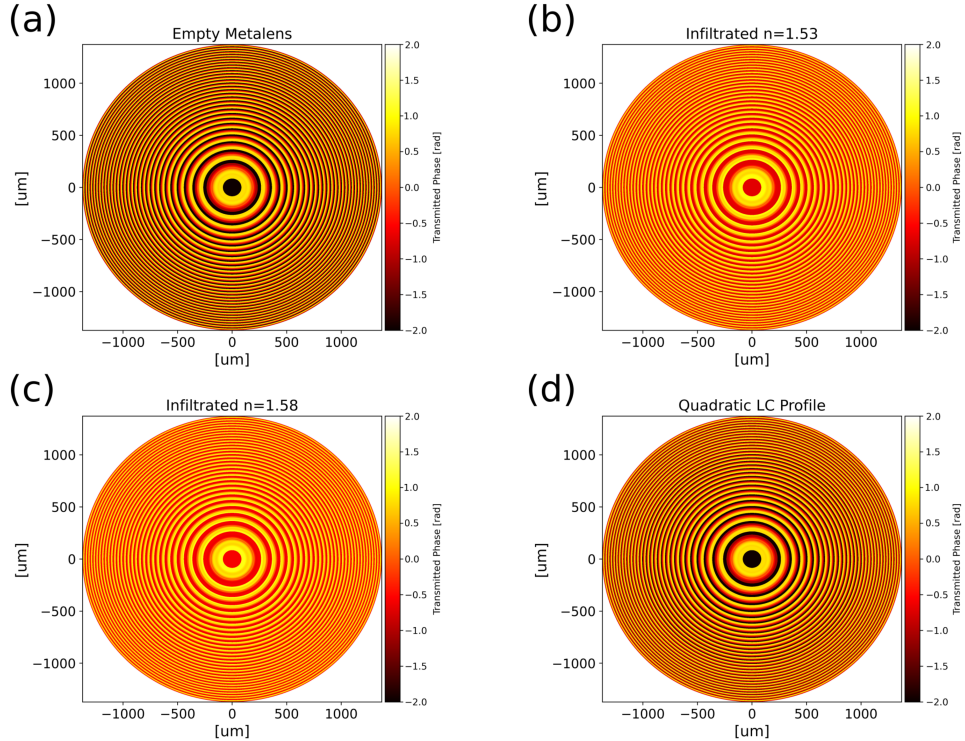


Figure S8: Transmitted phase in the near field for the metalens profile with various infiltration states: **(a)** Empty or uninfilitrated, **(b)** constant height of infiltration ( $0.25\mu\text{m}$ ) at refractive index 1.53, **(c)** constant height of infiltration ( $0.25\mu\text{m}$ ) at refractive index 1.58, and **(d)** a quadratic increasing infiltration profile increasing from  $0\mu\text{m}$  to  $0.5\mu\text{m}$  at a radial distance of  $3.75\text{ mm}$ . In this case the effects of the quadratic profile are minimal in the center, but can be seen near the edges. Only the central region of the metalens is shown, with a constant phase colormap. Note that any occurrence of secondary circular patterns is a result of an artifact of Moire patterns.

## Mechanism of coexisting phase profiles

We propose that the shift in the focal point can be explained by a mechanism of a total phase profile written as the sum of two individual phase profiles. The two phase profiles are those due to the geometric placement of the glass pillars, and the effects from the infiltrated liquid crystal. Thus the liquid crystal infiltration can serve either to (1) ‘wash out’ the phase difference provided by the pillars by depressing the index contrast or (2) introduce a secondary phase profile in the near field, or some combination of these effects.

An illustration of this point can be taken by considering the phase profiles and corresponding far field focusing behavior for several extreme cases. For a low LC infiltration state with index near the substrate index, the phase profile and far field focusing is similar to that of the empty metalens. This must be the case, since the empty structure is the limiting case of low infiltration. For relatively high and constant infiltration levels, the phase contrast is seen to decrease, as well as the intensity of the far field focusing profile. This case corresponds to an extreme case of (1) above, where the liquid crystal depresses the index contrast between the pillars and the surrounding medium and subsequently decreases the range of the transmitted phases, without the introduction of a significant spatially varying secondary profile. However, when we introduce a radial position dependent profile for the liquid crystal infiltration the opportunity to introduce a secondary phase profile arises, as in (2) above. The clearest case of this profile is a quadratically increasing infiltration height, with a diameter nearly equal to that of the entire metalens, and a relatively high maximum infiltration height. The infiltrated LC depth in this case approximates a refractive lens, with similar focal distance to the fabricated metalens. For this configuration, the far field presents as two focal points significantly separated from each other along the optical axis (both can be independently resolved). Such a double focusing profile can be described by the action of multiple lensing structures. A representation of this case can be seen in **Figure S10b** in the bottom panel, where the profile approaches that represented above. Finally we can consider the case presented in the main text, with a radius of 4.0 mm and a maximum infiltration height of  $0.8\mu\text{m}$ . This specific profile was chosen to correspond to experimental thickness measurements. In this case, the infiltration height

and radius are significant parameters in that they are large enough to induce a quadratic secondary phase profile from the liquid crystal (small radii approximate a uniform filling, while low heights approximate an empty lens), while still affecting the built-in phase profile significantly enough to shift the main focus rather than independently detuning from it. In the top four panels of **Figure S10a** we can see this effect as, for increasing infiltration depths, the focal point is seen to shift outward while still being well described by a single peak.

This effect can be seen more clearly in **Figure S9** and **Figure S10**, showing a comparison of far field intensity profiles for similar infiltration profiles (all quadratically increasing infiltration profiles similar to that shown in the main text). In each panel the radius of maximal infiltration is kept constant and the maximum height of infiltration is varied vertically from 10% to 50%. By increasing the maximum height at a constant radius we are effectively increasing the radial phase accumulation of the liquid crystal infiltrate for the chosen radial profile. This leads to an increase in focal distance for the secondary profile, and indeed the secondary focal spot can be seen to move apart from the primary focal spot located at the focal distance for the empty metalens. For clarity, the point of maximal focus has been plotted as a function of infiltration depth, for 4.75mm and 3.75mm radial profiles (**Figure S11**). The FWHM of the focal spot along the optical (z) axis is shown in red. From these figures it is clear that the single focal point is composed of two separate peaks, and tends to split into two at sufficient infiltration depth. However, for the radial profiles with a radius roughly less than 3.50mm, the second foci is diminished for greater infiltration depths, leading to a distorted single foci type profile.

We stress that the choice of phase profile for the case presented in the manuscript is not unique, in that there are potentially several infiltration profiles which could produce similar results. We have only studied quadratic increasing infiltration, and the effect is not excluded from other functional types. The main qualifications to produce this effect are those given above, namely a significant secondary phase profile, but not so far detuned as to leave the initial phase profile nearly unaffected. The case presented in the manuscript is physically motivated by previous experimental observations of the infiltration profile and the decreasing radial spacing designed into the metalens, however

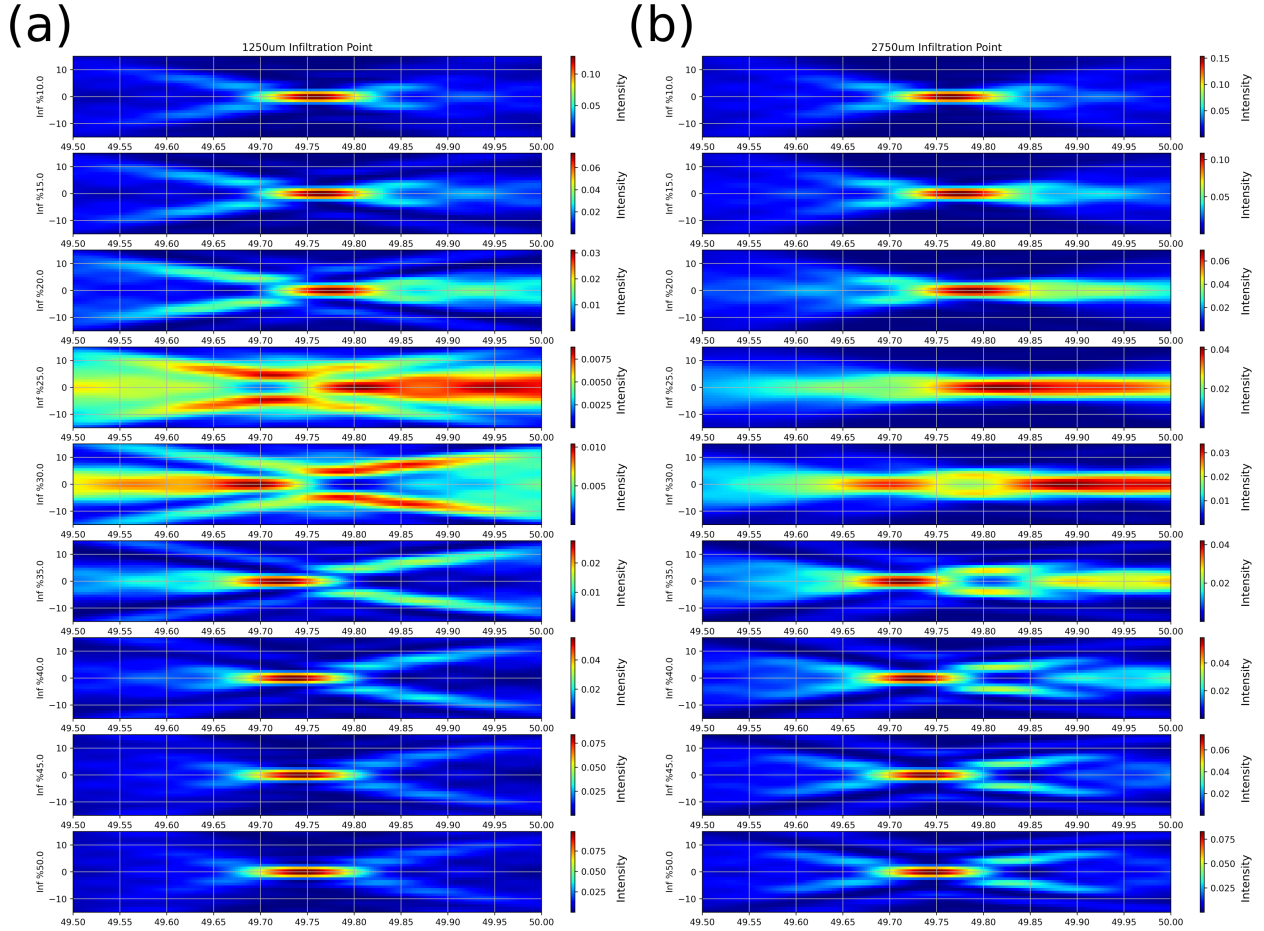


Figure S9: Comparison of the far field intensity focusing profiles for radial quadratic infiltration profiles with various parameters. The intensity is normalized to the incident field. Radial infiltration distances of (a)  $1250 \mu\text{m}$  and (b)  $2750 \mu\text{m}$  are constant in each column, with increasing maximum infiltration depth. The y-axis units are  $\mu\text{m}$  and the x-axis is in mm. The shifts in the focal distance along the optical axis (positive x direction) are clear.

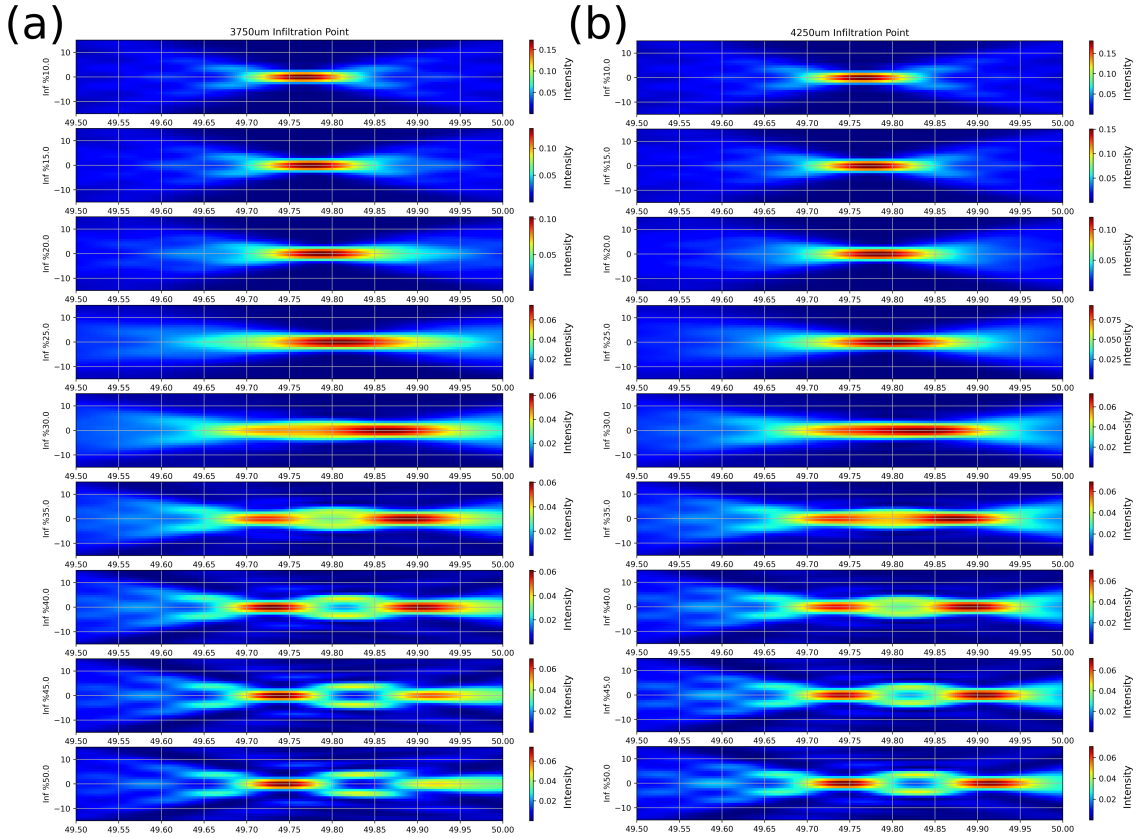


Figure S10: Comparison of the far field intensity focusing profiles for radial quadratic infiltration profiles with various parameters. The intensity is normalized to the incident field. Radial infiltration distances of **(a)**  $3750 \mu\text{m}$  and **(b)**  $4250 \mu\text{m}$  are constant in each column, with increasing maximum infiltration depth. The y-axis units are  $\mu\text{m}$  and the x-axis is in mm. The shifts in the focal distance along the optical axis (positive x direction) are clear. Additionally the appearance of a secondary focal spot with similar intensity is noted.

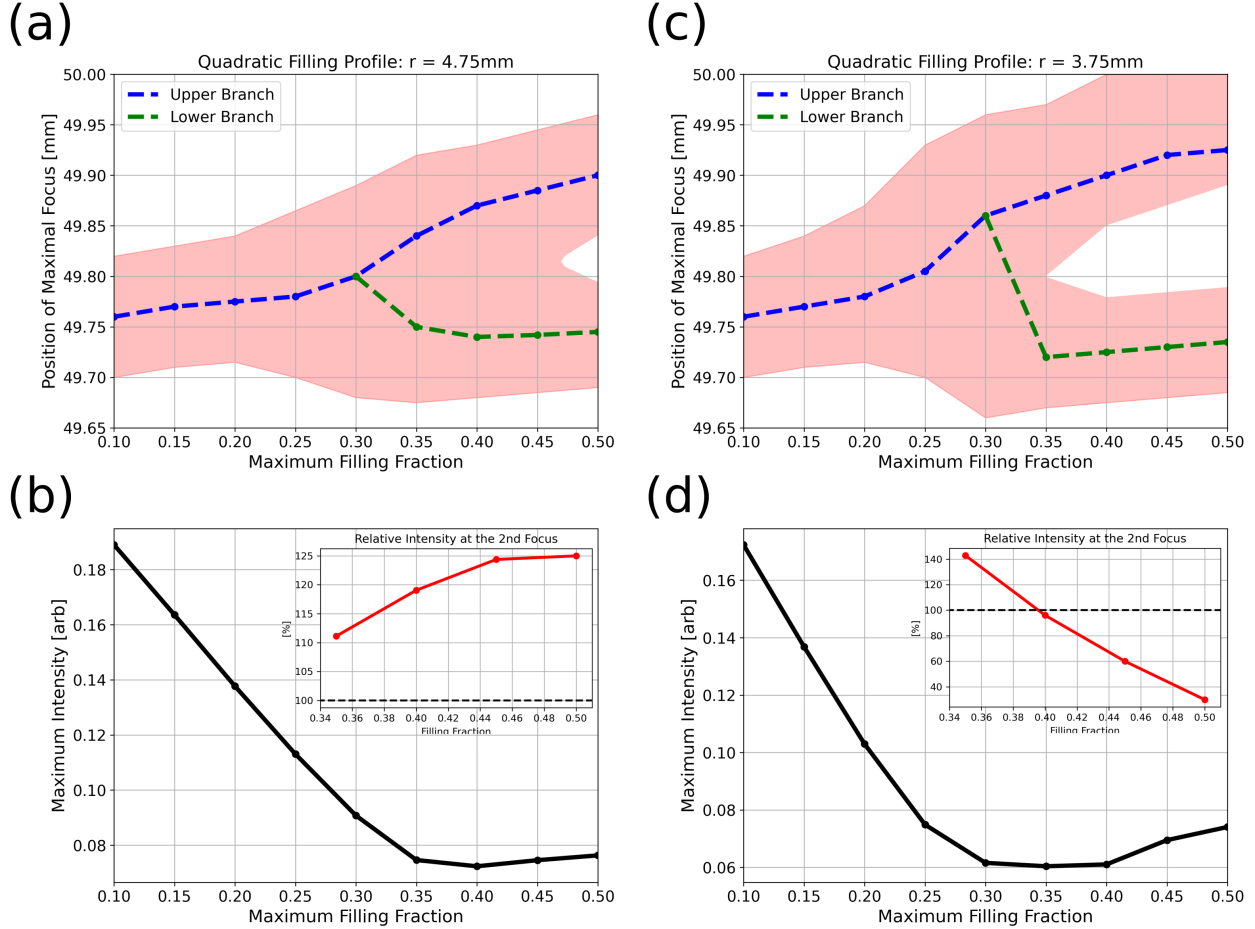


Figure S11: Focal distance shift for the far-field focusing profiles of radial distance **(a, b)** 4.75mm and **(c, d)** 3.75mm. The position of the maximal focus is shown along with the maximum intensity as a function of increasing filing fraction (depth of infiltration). The FWHM along the optical axis is shown in red. After roughly 30% depth, the focal spot can be resolved into two independent foci which shift apart in space. The breaking of the focal point is similarly illustrated by the decrease and plateau in maximum intensity values in the same range. **Inset** The distribution of intensity between the two focii is shown as a percentage of intensity at the second relative to the first focus (nearest the initial focal point).

other profiles could be present within the range of experiential error. Fundamentally, the micro to nanoscale details of the infiltration is unique for each individual experiment, which makes the determination of a single profile difficult. To illustrate this point even for radial quadratic profiles, a plot of the focal point shift distance for different radial infiltration profiles (in terms of radius of infiltration and maximum height) for the ordinary and isotropic refractive indices are shown in **Figure S14**.

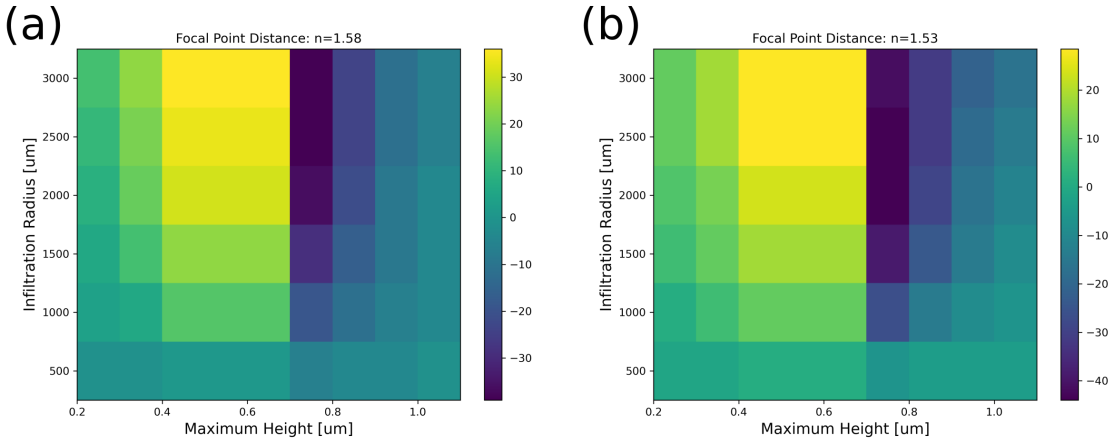


Figure S12: Shift in the focal point distance ( $\mu\text{m}$ ) for various parameters of the quadratic radial infiltration, simulated for the **(a)** isotropic LC refractive index (1.53) and **(b)** the ordinary index (1.53). Only smaller infiltration radii are shown, where the occurrence of a secondary focal point is minimized. Clear shifts in the focal distance on the order of  $30\text{-}40\mu\text{m}$  are observed, with a large shift in the range of  $0.40\mu\text{m}$  to  $0.80\mu\text{m}$  depth. The effect of changing refractive index is notable, but small compared with the changing profile parameters.

## Manipulating the Focal Point Tunability Range by Varying the Infiltrate Refractive Index

It is stated in the manuscript that the nanoscale pillar arrangement of the metasurface is not optimized to support a liquid crystal infiltrate. This applies to both the far-field focusing and focal point tunability properties. However, we expect that a similar optical metasurface could be designed to optimize both of these properties while maintaining the current schema of inter-pillar liquid crystal infiltration. Additional simulations have been performed to illustrate that the focal point tunability of the presented metasurface could indeed be optimized beyond the current performance. The pillar geometry of the base metasurface has been maintained in these simulations, while the refractive index of the infiltrated liquid crystal is continually tuned from 1.0 to 1.6. A range of infiltration profiles are considered. The base metasurface has been previously optimized for focusing without infiltration (target infiltrate of  $n = 1.0$ ). By tuning the liquid crystal refractive index away from the optimal value, locally optimal refractive indices can potentially be found for specific infiltration profiles. This protocol is the converse to altering the base metasurface to manipulate the target infiltrate refractive index for a fixed liquid crystal refractive index ( $\sim 1.55$  for typical liquid crystals).

The focal point shift obtained by manipulating the liquid crystal refractive index and the maximum infiltrated height is shown for both constant (**Figure S13 a**) and radially varying (**Figure S13 b**) infiltration profiles. The radially varying infiltration profiles are similar to that considered in the manuscript. All focal distances are presented as  $\mu m$  shifts from the focal point of the uninfiltrated lens ( $n = 1.0$ ). From **Figure S13 a**, we expect that a focal point shift tunability of  $> 100 \mu m$  can be reached by manipulating the refractive index and infiltrated height of the liquid crystal, without changing the infiltration profile. This is greater than the simulated focal point shift for the experimental liquid crystal refractive indices. Note that birefringence on the order of 0.2 to 0.3 can be found in a range of commercially available liquid crystals, so these refractive index shifts reasonable. Comparing the range of focal point shifts available for various infiltration heights at  $n = 1.5$  (the nearest simulated value for typical liquid crystals), the focal point shift is notably smaller than those obtained at lower refractive index values. If the refractive indices are considered as relative to the target refractive index, this result suggests that a metalens designed for optimized focusing at a target infiltrate refractive index of  $n = 1.2$  ( $\Delta n \sim 0.3$ ) would produce a larger focal point shift in comparison with the metalens presented in the manuscript. A wide range of positive focal point shifts can be seen in **Figure S13 b**, where the increased range is a result of the radially quadratic infiltration profile. Note that in cases where double focii are observed, as discussed in previous sections of the supplementary, the primary (strongest and most enduring) focal peak is reported. In this case the focal point shift could be increased by lowering the maximum infiltrated height and increasing the refractive index of the infiltrated liquid crystal. Allowing for infiltration profile changes,  $> 100 \mu m$  shifts can be obtained for a range of refractive indices.

Finally, it should be noted that these simulations maintain the initial un-infiltrated lens structure. The nanoscale pillar geometry is critical to the tunability ranges and focusing profile. These results should not be taken as limitations to the focal point tunability range but rather as an illustration that the device could indeed be better optimized for increased focal point shift. Such optimization could occur by manipulating the nanostructure of the base lens, which has the potential to drastically increase the focal point tunability range.

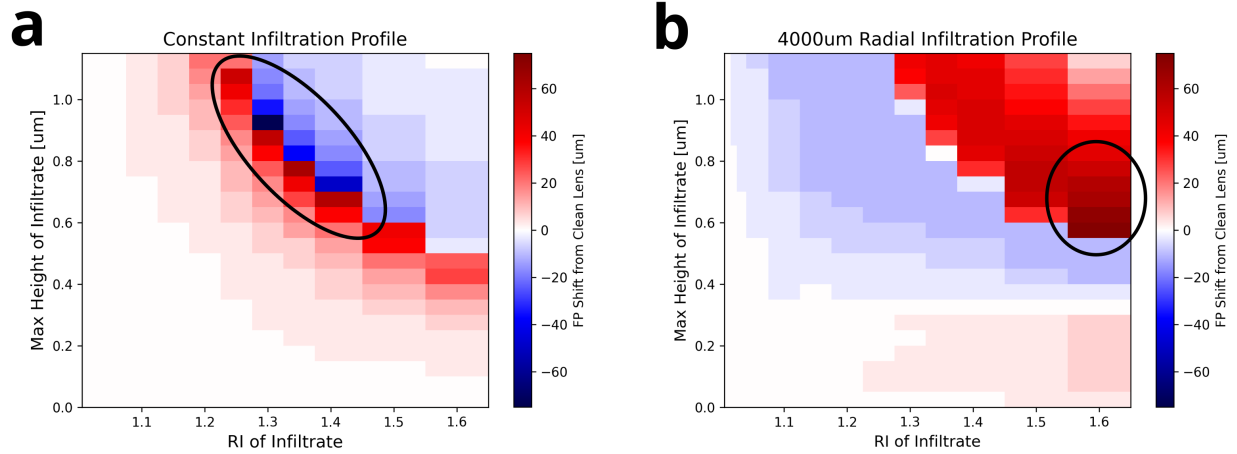


Figure S13: Simulated focal point comparison for a range of infiltrate (NLC) refractive index and infiltration profiles. Focal point is given as the difference from that of the clean, uninfiltrated lens. Both **a** smooth and **b** radially varying infiltration profiles are considered. The radial profile is similar to the profile considered in the manuscript. The regions of greatest focal point shift are circled in black.

### Experimental estimation of the infiltrated liquid crystal thickness

The equilibrium LC profile following the NLC infiltration shows a non-uniform, non-zero infiltration height over the metalens extent. The infiltrated height of the LC film ( $t$ ) has been measured with a tilt optical delay compensator, which relates the phase retardation ( $\Gamma$ ) and birefringence ( $\Delta n$ ) to the film thickness ( $\Gamma = t\Delta n$ ). In the nematic phase, the LC follows a generally quadratically increasing radial infiltration profile, starting from  $\sim 15\%$  of the pillar height and reaching a maximum of  $\sim 40\%$  at 3.95mm radially from the center. This infiltration profile is expected, as discussed in the main text, and is indicative of the complex radially non-uniform pillar geometry of the metasurface substrate. Additionally, specifics of the infiltration procedure can lead to divergences in the infiltrated film height between independent experimental infiltration attempts.

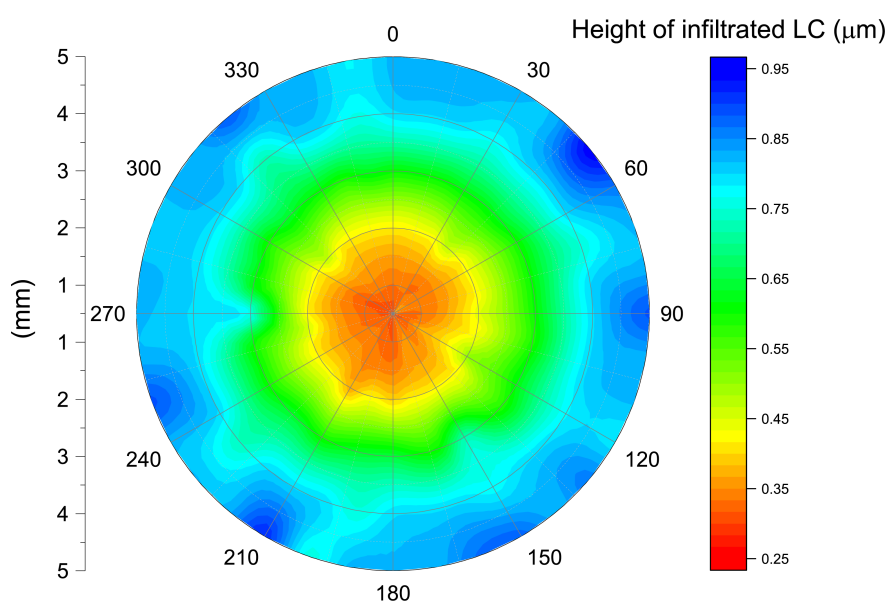


Figure S14: Infiltrated nematic liquid crystal thickness within the metalens structure 24hours after the NLC infiltration procedure.

## Comparison with Some Other Similar Tunable Metalens Systems

A brief table is presented comparing the results from this work with several recent varifocal metalens systems. Comparisons include: tunable mechanism, range of tunability and quality of focus, operation wavelength, and design specifics such as the optimality of the design and the use of a thick bulk layer. Note that this table is not exhaustive of varifocal metalens devices and other such systems do exist. We have attempted to show several systems with the most similarity to the system presented in this work, focusing on liquid crystal based devices.

Title	Control Method	Tunability Range	Focusing Quality	Wavel. Range	Optimized Design	Bulk LC?
<b>This work</b>	Liquid Crystal: Opto-thermal excitation of the nematic - isotropic transition	0.16% of 5cm	SR: 0.31 / 0.39	Visible	No	No
<b>Electrically Actuated Varifocal Lens Based on Liquid-Crystal-Embedded Dielectric Metasurfaces.</b> (Bosch, et. al.)	Liquid Crystal: Electrically controlled tilt angle in an embedded cell geometry	20% of 15mm	SR: 0.75 / 0.84	Visible	Yes	Yes
<b>Electrically Driven Varifocal Silicon Metalens</b> (Afriadi et. al.)	Electrical resistive heating of a silicon on quartz system	15% of 600um 23% of 1000um	SR: 0.66 / 0.67	Visible	Yes	No
<b>Electrically Modulated Varifocal Metalens Combined with Twisted Nematic Liquid Crystals</b> (Fan et. al.)	Liquid Crystal: Electrically controlled twist angle in a cell geometry	70% of 45um	FE: 40% / 70%	Visible	Yes	Yes
<b>Liquid Crystal Integrated Metalens with Tunable Chromatic Aberration</b> (Shen et. al.)	Liquid Crystal: Electrically controlled tilt angle in a cell geometry	N/A chromatic aberration vs. focal point shift of 15mm	FE: 34% / 26%	THz	Yes	Yes
<b>Electrically Tunable Terahertz Focusing Modulator Enabled by Liquid Crystal Integrated Dielectric Metasurface</b> (Shen et. al.)	Liquid Crystal: Electrically controlled tilt angle in an embedded cell geometry	21% of 10.5mm	FWHM: 514um / 428um	THz	Yes	Yes
<b>Electrically Driven Zoom Metalens Based on Dynamically Controlling the Phase of BTO Column Antennas</b> (Xu et. al.)	BTO: Electrically controlling the refractive index of BTO nanopillars	80% of 50um	FWHM: 0.56um	Visible	Yes	No
<b>Reconfigurable All Dielectric Metalens with Diffraction Limited Performance</b> (Shalaginov et. al.)	PCM: Phase change in GSST phase change material	25% of 2mm	FE: 39% / 25%	IR	Yes	No

Figure S15: Comparison of this work with several other recent tunable metalens systems.

## References

- (1) Li, J.; Gauzia, S.; Wu, S.-T. High temperature-gradient refractive index liquid crystals. *Optics express* **2004**, *12*, 2002–2010.
- (2) Bastús, N. G.; Comenge, J.; Puntes, V. Kinetically controlled seeded growth synthesis of citrate-stabilized gold nanoparticles of up to 200 nm: size focusing versus Ostwald ripening. *Langmuir* **2011**, *27*, 11098–11105.
- (3) Oskooi, A. F.; Roundy, D.; Ibanescu, M.; Bermel, P.; Joannopoulos, J. D.; Johnson, S. G. MEEP: A flexible free-software package for electromagnetic simulations by the FDTD method. *Computer Physics Communications* **2010**, *181*, 687–702.